Ab Initio Derivation of Lattice-Gauge-Theory Dynamics for Cold Gases in Optical Lattices

Federica Maria Surace,[1,*] Pierre Fromholz,[2,3,†] Nelson Darkwah Oppong,[4,5,§]
Marcello Dalmonte,[2,3] and Monika Aidelsburger[4,5,‡]

[1] *Department of Physics and Institute for Quantum Information and Matter, California Institute of Technology, Pasadena, California 91125, USA*
[2] *The Abdus Salam International Centre for Theoretical Physics (ICTP), strada Costiera 11, Trieste 34151, Italy*
[3] *International School for Advanced Studies (SISSA), via Bonomea 265, Trieste 34136, Italy*
[4] *Faculty of Physics, Ludwig-Maximilians-Universität München, Schellingstr. 4, Munich D-80799, Germany*
[5] *Munich Center for Quantum Science and Technology (MCQST), Schellingstr. 4, Munich D-80799, Germany*

(Received 23 January 2023; accepted 19 April 2023; published 24 May 2023)

We introduce a method for quantum simulation of U(1) lattice gauge theories coupled to matter, utilizing alkaline-earth(-like) atoms in state-dependent optical lattices. The proposal enables the study of both gauge and fermionic matter fields without integrating out one of them in one and two dimensions. We focus on a realistic and robust implementation that utilizes the long-lived metastable clock state available in alkaline-earth(-like) atomic species. Starting from an *ab initio* modeling of the experimental setting, we systematically carry out a derivation of the target U(1) gauge theory. This approach allows us to identify and address conceptual and practical challenges for the implementation of lattice gauge theories that—while pivotal for a successful implementation—have never been rigorously addressed in the literature: those include the specific engineering of lattice potentials to achieve the desired structure of Wannier functions and the subtleties involved in realizing the proper separation of energy scales to enable gauge-invariant dynamics. We discuss realistic experiments that can be carried out within such a platform using the fermionic isotope ^{173}Yb, addressing via simulations all key sources of imperfections, and provide concrete parameter estimates for relevant energy scales in both one- and two-dimensional settings.

DOI: 10.1103/PRXQuantum.4.020330

I. INTRODUCTION

In the past decade, the rapid development of quantum simulators has motivated an increasingly large interest in possible applications to nuclear and particle physics. The study of lattice gauge theories (LGTs) [1–3], one of the most successful theoretical frameworks to regularize strong-interacting-field theories, could take great advantage of the use of quantum devices. First formulated in the 1970s [1], classical simulations of LGTs based on Monte Carlo sampling soon became a pillar of our understanding of quantum chromodynamics (QCD) [3], with applications as diverse as low-energy spectra [4,5], phase diagrams [6–8], and even precision measurements in the context of the recently puzzling muon-magnetic-moment results [9]. Quantum simulators promise to extend our understanding of LGTs to regimes that are presently inaccessible to Monte Carlo methods, including real-time dynamics or the physics of the early universe and neutron stars [10–15].

Starting from early theoretical proposals, the field of quantum simulation of LGTs has evolved rapidly, driven by two factors: the development of quantum simulation tools and schemes tailored to the specificity of gauge theories (in particular, gauge invariance), and a series of first experimental steps that have been taken to demonstrate the feasibility of the proposed schemes. The former has been pioneered by the trapped-ion experiment reported in Ref. [16] (later extended in Ref. [17]), where the dynamics of a few-site Schwinger model [i.e., quantum electrodynamics in (1+1) dimensions] with up to six sites have been

---

[*] fsurace@caltech.edu
[†] pierre.fromholz@unibas.ch
[‡] monika.aidelsburger@physik.uni-muenchen.de
[§] Current address: JILA, University of Colorado and National Institute of Standards and Technology, and Department of Physics, University of Colorado, Boulder, Colorado 80309, USA

demonstrated. Moreover, building blocks of matter-gauge interactions have been successfully demonstrated in cold-atom settings, including both $\mathbb{Z}_2$ [18] and U(1) [19] gauge theories in one dimension (1D), utilizing the quantum link formulation (QLM) of LGTs, where the dimension of the local Hilbert space of the gauge link is truncated and therefore finite. More recently, large-scale quantum simulations of Abelian LGTs have been reported in Rydberg-atom arrays (Schwinger model [20,21], as well as a (2+1)D Ising-Higgs gauge theory [22]) and with ultracold bosonic atoms in tilted optical superlattices [23–25]. In the continuum, quantum simulation of a topological gauge theory has been realized in an optically dressed Bose-Einstein condensate by realizing a 1D reduction of the Chern-Simons theory, the so-called chiral BF theory [26].

The first generation of experimental realizations has already proven that quantum simulators of LGTs can reach system sizes and time scales at the boundaries of the capabilities of classical numerical simulations [20,21]. Nevertheless, many challenges still have to be overcome before we can utilize quantum devices for making accurate predictions on complex gauge theories such as QCD. Despite the recent experimental progress mentioned above, it remains unclear whether quantum simulators can satisfy the requirements for quantum simulation of LGTs with fermionic matter in more than one dimension [27]: digital quantum simulation schemes are hampered by the limited system sizes and the large number of gates needed to simulate such complex models; analog quantum simulators, on the other hand, reach larger system sizes but are typically not flexible enough to simulate the desired models.

Various strategies can be used to facilitate the implementation of LGTs in a quantum simulator. In the pioneering experiments implemented with trapped ions [16,17], gauge fields are eliminated by a Jordan-Wigner transformation, which maps the original Schwinger model to a spin model with exotic long-range interactions. Gauge elimination has later been used in other digital schemes to simulate non-Abelian LGTs in one spatial dimension [28,29]. A related approach is followed for implementations of QLMs in Rydberg atom arrays, where the matter fields are integrated out [21]. While gauge integration is only possible in one spatial dimension, matter integration (or similar strategies that utilize the gauge redundancy to reduce the number of degrees of freedom) can also often be used to simplify the protocol in higher dimensions [30,31], without compromising the physical properties of the model. However, in some cases, matter integration is not possible (e.g., in models with multiple matter species) or introduces additional constraints and longer-range terms that are challenging to implement in a physical system [32]. It can therefore be more convenient to apply the initial strategy of keeping both matter and gauge fields. This is particularly true for the case of analog quantum simulators, where it is often useful to focus on more “natural” implementations at the price of a larger number of degrees of freedom.

Most proposals for simulating both (fermionic) matter and (bosonic) gauge fields require implementations based on ultracold mixtures [19], which significantly increases the experimental complexity. QLMs, on the other hand, are characterized by a finite-dimensional Hilbert space for the gauge degrees of freedom, offering the possibility of implementing matter and gauge degrees of freedom with a single atomic species. This has been demonstrated with ultracold bosons in tilted optical superlattice potentials [23–25] and a possible extension of this scheme to higher dimensions is currently being explored theoretically [33]. Moreover, schemes based on Floquet engineering appear challenging due to the presence of higher-order terms that need to be suppressed in order to respect gauge invariance [18], e.g., by implementations of additional stabilizers [34]. In order to overcome these limitations, we develop a new scheme for the realization of U(1) QLMs with ultracold alkaline-earth(-like) atoms (AELAs) that offers a direct implementation of fermionic matter and gauge fields, as well as a straightforward extension to two dimensions.

To ensure a robust experimental implementation, it is crucial to further bridge the gap between theoretical proposals, which focus on conceptual developments and novel implementation schemes, and experimental realizations, which require microscopic derivations of the gauge-theory dynamics. The last step is vital in order to understand at a qualitative and quantitative level the impact of often-neglected challenges or even roadblocks—including particle losses, limited coherence time (e.g., due to spontaneous emission), and practical difficulties (such as challenges in realizing the required optical potentials).

In this work, we introduce a novel scheme and present an *ab initio* derivation of a U(1) lattice gauge theory in both one and two spatial dimensions using AELAs in optical lattices. The backbone framework is an implementation that relies on protecting gauge invariance utilizing a combination of energy penalty and locality, through a specific design of state-dependent optical potentials that are particularly well suited for atomic species with a long-lived electronically excited state [35,36]. We carry out a thorough numerical study of the experimental parameters of the optical lattice needed to obtain a regime for our quantum simulation that features the best ratio between coherent and incoherent dynamics. We compute the parameters of the lattice model and simulate the corresponding microscopic dynamics, showing that a moderate amount of on-site disorder would only mildly affect the observed time evolution.

II. QUANTUM LINK MODEL

In this work, we focus on the realization of a U(1) lattice gauge theory with fermionic matter, the lattice version of the Schwinger model, i.e., quantum electrodynamics in one spatial dimension [37]. Despite its simplicity, the Schwinger model displays several salient features in common with more complicated ones, including confinement, chiral symmetry breaking, and nontrivial real-time dynamics [38].

In one spatial dimension, the Hamiltonian has the form [2]

$$H_{\mathrm{LGT}} = -w\sum_j \left(\psi_j^\dagger U_{j,j+1}\psi_{j+1} + \mathrm{H.c.}\right) + m\sum_j (-1)^j\,\psi_j^\dagger\psi_j + g\sum_j (E_{j,j+1}+\mathcal{E}_0)^2, \quad (1)$$

where $\psi_j^\dagger$ and ψ_j are fermionic creation and annihilation operators on site j of a 1D lattice. The operators $U_{j,j+1}$ and $E_{j,j+1}$ are, respectively, the parallel transporter and the electric field operators, with commutation relation $[E_{i,i+1}, U_{j,j+1}] = \delta_{ij}\, U_{j,j+1}$: these operators represent a U(1) gauge field on the link connecting the sites j and $j+1$. The nearest-neighbor hopping term, of amplitude w, is made gauge invariant by the parallel transporter $U_{j,j+1}$. The fermionic mass is staggered, according to the Kogut-Susskind formulation [39,40]: on even sites, an occupied fermionic site represents a "positron" with charge $+1$, while "electrons," of charge -1, are represented by holes on odd sites [Fig. 1(c)]. We can therefore define the local charge as

$$q_j = \psi_j^\dagger\psi_j - \frac{1-(-1)^j}{2}. \quad (2)$$

The mass term in Eq. (1) assigns the mass m to both electrons and positrons. Finally, the term proportional to g is the energy of the electric field and $\mathcal{E}_0$ represents a static background electric field. The Hamiltonian in Eq. (1) has a gauge symmetry generated by the local operators G_j, defined as

$$G_j = E_{j,j+1} - E_{j-1,j} - q_j\,. \quad (3)$$

In the absence of static charges, the physical states for the LGT are those that satisfy the local constraint (*Gauss's law*) $G_j\,|\Psi\rangle = 0$ for every site j.

In the following, we consider the quantum link formulation of the model [41–44]: in this formulation, all the gauge fields are represented by a finite d-dimensional Hilbert space (we choose $d = 2$) and the operators $E_{j,j+1}$ and $U_{j,j+1}$ have the form of S^z and S^+ operators, respectively. In the limit of large d (with $d = 2s+1$, where s is the spin representation), this formulation is equivalent to the usual Wilsonian lattice-gauge theories [1,2], where the electric field has an unbounded integer spectrum. Compared to the latter, the quantum link formulation is particularly suitable for quantum simulations, because it exploits finite-dimensional quantum degrees of freedom.

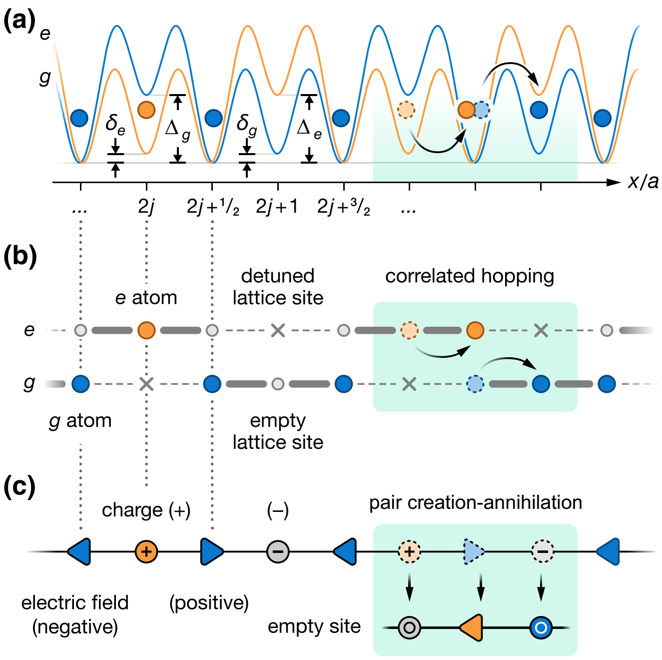

FIG. 1. The mapping between atomic states in the optical-lattice potential and the U(1) quantum link model considered in our proposal. (a) A schematic of the optical-lattice potentials for the g (blue line) and e atoms (orange line), together with the relevant energy scales $\delta_{g,e}$ and $\Delta_{g,e}$. The circles indicate an exemplary initial state of g (blue circles) and e atoms (orange circles) in the optical lattice. The black arrows on the right indicate the correlated hopping of atoms between adjacent lattice sites. (b) A simplified schematic of the optical-lattice potential in (a) showing the bonds across which hopping is energetically allowed (thick gray lines) and forbidden (dashed gray lines). (c) The state in the quantum link model corresponding to the atomic configuration in (a) and (b). In the mapping, every lattice site that can only be occupied by e or g atoms is interpreted as a matter site, shown as circles, with the plus (+) [minus (−)] labels indicating filled sites with positive (+) [negative (−)] charge. The lattice sites that can be occupied by both e and g are interpreted as link (l) or gauge-field sites, where the triangles pointing right (left) indicate a positive (negative) electric field. The colors indicate the corresponding internal state of the atoms [see (a) and (b)] in the proposed experimental implementation and gray indicates an empty site. Note that the correlated hopping of atoms is mapped to a gauge-invariant pair creation-annihilation process, as shown on the right.

Here, we focus on the spin-1/2 representation [45]. In this case, the electric field has the two possible values $E_{j,j+1} = \pm 1/2$ [Fig. 1(c)], which have the same energy for $\mathcal{E}_0 = 0$. This choice, with half-integer values of the electric field, is generally denoted as having a *topological angle* $\theta = \pi$ (in contrast to the case of integer electric field values, having $\theta = 0$) [21]. The topological angle can be tuned by changing the static background field $\mathcal{E}_0$, the effect of which is to split the degeneracy between the two electric field states [46,47]. For the spin-1/2 representation, it is useful to define $\tau = 2g\mathcal{E}_0$. Then, the Hamiltonian given in Eq. (1) becomes (up to an additive constant)

$$H_{\rm QLM} = -w \sum_j \left(\psi_j^\dagger U_{j,j+1} \psi_{j+1} + \text{H.c.} \right) + m \sum_j (-1)^j \psi_j^\dagger \psi_j + \tau \sum_j E_{j,j+1}. \quad (4)$$

With this notation, choosing $\tau \neq 0$ effectively changes the topological angle to $\theta \neq \pi$. We note that the above model can be exactly mapped to a spin chain via direct integration of Gauss's law [21].

III. QUANTUM SIMULATION

A. Optical lattice

In the proposed experimental setup, we consider cold fermionic atoms in two different electronic states $\alpha = \{g, e\}$, realized by the ground and metastable excited clock states $g \equiv {}^1S_0$ and $e \equiv {}^3P_0$ of AELAs. The atoms are considered to be spin polarized in a given nuclear Zeeman state m_F, so that the corresponding Hamiltonian is given by $H = H_{\rm nonint} + H_{\rm int}$, with [48]

$$H_{\rm nonint} = \sum_\alpha \int d^3\mathbf{r} \Psi_\alpha^\dagger(\mathbf{r}) \left(-\frac{\hbar^2}{2M} \nabla^2 + V_\alpha(\mathbf{r}) \right) \Psi_\alpha(\mathbf{r}),$$
$$H_{\rm int} = g_{eg}^- \int d^3\mathbf{r} \rho_e(\mathbf{r}) \rho_g(\mathbf{r}). \quad (5)$$

Here, $\Psi_\alpha(\mathbf{r})$ denotes the fermion field operator for atoms in the internal state $|\alpha\, m_F\rangle$. The density operators are defined as $\rho_\alpha(\mathbf{r}) = \Psi_\alpha^\dagger(\mathbf{r})\Psi_\alpha(\mathbf{r})$. Since the atoms are polarized in the same nuclear Zeeman state, the interaction strength, $g_{eg}^- = 4\pi\hbar^2 a_{eg}^-/M$ (where M is the atomic mass), is associated with the scattering length a_{eg}^- of the antisymmetric electronic state [49,50]. The term $V_\alpha(\mathbf{r})$ denotes a three-dimensional (3D) lattice potential $V_\alpha(\mathbf{r}) = V_\alpha^x(x) + V_\alpha^y(y) + V_\alpha^z(z)$, where $V_\alpha^x(x)$ is the state-dependent potential depicted in Fig. 1(a) and $V_\alpha^y(y)$ and $V_\alpha^z(z)$ are deep state-independent optical lattices with amplitude $F_g = F_e$ and lattice spacing $d_y = d_z$ that isolate individual 1D chains and provide strong radial confinement. For simplicity, we choose equal amplitudes for the transverse lattices along y and z. The state-dependent lattice along x is defined as

$$V_\alpha^x(x) = -A_\alpha \sin^2\left(\frac{\pi}{2a}x + \varphi\right) - B_\alpha \sin^2\left(\frac{\pi}{a}x\right) - C_\alpha \sin^2\left(\frac{2\pi}{a}x + \frac{\pi}{2}\right). \quad (6)$$

It has a unit cell of length $2a$ with three "low"-energy lattice sites and one "high"-energy site, which suppresses tunneling to that site, as shown schematically in Fig. 1(b). The triple wells of the g and e lattices are shifted relative to each other by a distance a.

The optical potential along x can be realized by superimposing three different optical lattices. Each of them is generated from a pair of monochromatic laser beams at either the magic wavelength λ_m [51,52], which corresponds to a state-independent potential, or the antimagic wavelength λ_{am} [53], where the potentials for atoms in the g and e states are equal in magnitude but have opposite signs. Moreover, the lattice spacing can be set by tuning the intersection angle θ between the interfering pair of laser beams according to $\lambda/[2\sin(\theta/2)]$. The two shorter-spacing lattices in Eq. (6) are operated at the magic wavelength λ_m ($B_e = B_g$ and $C_e = C_g$) and at intersection angles $\theta_C = 180^\circ$ and $\theta_B = 60^\circ$. The corresponding lattice spacings are $a = \lambda_m/2$ and $2a$, such that their combination yields a symmetric double-well potential [54,55]. The third long lattice at lattice spacing $4a$, which can be generated at a smaller intersection angle, is operated at λ_{am}, with $A_g = -A_e$ generating a triple-well potential that is shifted for g and e atoms as shown in Fig. 1(a) for $\varphi = 0$. Experimentally, the superposition of multiple optical lattices has been used in numerous quantum simulation experiments. The main challenge for our proposal is to realize a phase-stable realization of interfering optical lattices. While this is technically challenging, interfering lattices have been successfully demonstrated for a variety of complex lattice geometries with high phase stability (see, e.g., Refs. [56–60]). Note that the required optical potentials could also be generated using a hybrid approach using a combination of optical lattices and tweezers, which have recently been employed for Hubbard-type physics [61,62].

B. Lattice Hamiltonian

To obtain a lattice Hamiltonian for the model, we assume that only the three lowest Bloch bands are occupied both for the g and e states and we express the field operator $\Psi_\alpha(\mathbf{r})$ in terms of the Wannier functions $w_{\alpha,s}$, where $s = \{-, 0, +\}$ labels the three Wannier centers in a unit cell (Fig. 2):

$$\Psi_g(\mathbf{r}) = \sum_{j\ \text{odd}} \left[w_{g,+}(\mathbf{r} - \mathbf{r}_j) c_{j+1/2} + w_{g,0}(\mathbf{r} - \mathbf{r}_j) c_j + w_{g,-}(\mathbf{r} - \mathbf{r}_j) c_{j-1/2} \right], \quad (7)$$

$$\Psi_e(\mathbf{r}) = \sum_{j\ \text{even}} \left[w_{e,+}(\mathbf{r} - \mathbf{r}_j) d_{j+1/2} + w_{e,0}(\mathbf{r} - \mathbf{r}_j) d_j + w_{e,-}(\mathbf{r} - \mathbf{r}_j) d_{j-1/2} \right], \quad (8)$$

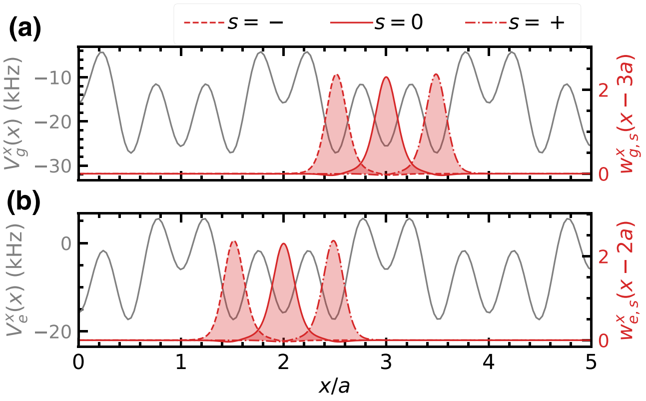

FIG. 2. The optical-lattice potential and the Wannier functions. The x component of the optical-lattice potential defined in Eq. (6) for the (a) g and (b) e atoms is plotted in gray for $\varphi = 0$. The parameters A_α, B_α, and C_α are reported in Table I. The x components of the Wannier functions centered on sites $x = 3a$ and $x = 2a$ are shown in red. The parameter $s = \{-, 0, +\}$ labels the three different orbitals in the unit cell.

where $\mathbf{r}_j = ja\hat{x}$, $\hat{x}$ is the unit vector, and c_j (d_j) is the lattice fermionic annihilation operator of a g atom (e atom) on lattice site j.

Substituting the expressions for the field operators in Eq. (5), we obtain the lattice Hamiltonian (see Appendix A),

$$H_{\text{latt}} = H_g + H_e + H_U + H_D + H_{\text{lr}} + \text{const}, \tag{9}$$

where H_g and H_e denote the terms containing hopping and chemical potentials of the g and e atoms within a single triple well, respectively:

$$H_g = \sum_{j\ \text{odd}} \left[-t_g \left(c_j^\dagger c_{j+1/2} + c_j^\dagger c_{j-1/2} + \text{H.c.} \right) + \delta_g c_j^\dagger c_j \right], \tag{10}$$

$$H_e = \sum_{j\ \text{even}} \left[-t_e \left(d_j^\dagger d_{j+1/2} + d_j^\dagger d_{j-1/2} + \text{H.c.} \right) + \delta_e d_j^\dagger d_j \right]. \tag{11}$$

We assume, for the moment, that $\varphi = 0$, so the model is symmetric under reflections centered on the matter sites: this implies that the chemical potentials of the sites $s = +$ and $s = -$ are the same (and can be chosen as a reference level and set to zero).

TABLE I. The experimental parameters. All values are given in units of $h \times$ kHz.

$A_g = -A_e$	$B_g = B_e$	$C_g = C_e$
9.827	6.343	15.832

$\Delta_g = \Delta_e$	$\delta_g = \delta_e$	U	$t_g = t_e$	$D_g = D_e$
7.22	1.02	2.03	0.085	0.023

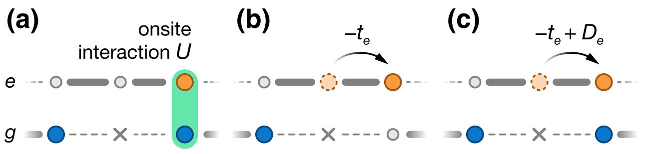

FIG. 3. The interacting terms in H_U and H_D. (a) The on-site interaction U between a single g (blue circle) and e atom (orange circle). (b) The hopping of a single e atom to an empty lattice site. (c) In the presence of interactions, tunneling is additionally modified by a density-assisted tunneling with amplitude D_e.

The terms H_U and H_D are obtained from the interacting term in Eq. (5) and read (see Fig. 3)

$$H_U = U \sum_j d_{j+1/2}^\dagger d_{j+1/2} c_{j+1/2}^\dagger c_{j+1/2}, \tag{12}$$

$$\begin{aligned} H_D = D_g \sum_{j\ \text{odd}} \Big(& d_{j+1/2}^\dagger d_{j+1/2} c_j^\dagger c_{j+1/2} \\ & + d_{j-1/2}^\dagger d_{j-1/2} c_j^\dagger c_{j-1/2} + \text{H.c.} \Big) \\ + D_e \sum_{j\ \text{even}} \Big(& c_{j+1/2}^\dagger c_{j+1/2} d_j^\dagger d_{j+1/2} \\ & + c_{j-1/2}^\dagger c_{j-1/2} d_j^\dagger d_{j-1/2} + \text{H.c.} \Big). \end{aligned} \tag{13}$$

Finally, H_{lr} contains all the additional terms, of the form of longer-range hoppings and interactions, that have very small amplitudes and can be neglected (we explicitly verify that these terms are negligible for the parameters reported in Sec. IV A). Note that we do not neglect the interaction terms in H_D (which are usually not included in simple Hubbard-like models) because these terms have a non-negligible effect on the QLM Hamiltonian for the realistic experimental parameters that we consider in Sec. IV A.

It is useful to define $\epsilon = (\delta_g - \delta_e)/2$, $\delta = (\delta_g + \delta_e)/2$, and the total number of atoms on each site $j + 1/2$, which corresponds to a link in the QLM (Fig. 1),

$$n_{j+1/2}^{(l)} = d_{j+1/2}^\dagger d_{j+1/2} + c_{j+1/2}^\dagger c_{j+1/2}. \tag{14}$$

Here, (l) is a redundant superscript to indicate that we are on a link. We now assume that the three parameters ϵ, t_α, and D_α are small compared to both δ and $U - \delta$: in this regime, it is convenient to split the Hamiltonian into three parts, $H_{\text{latt}} = H_0 + H_1 + H_{\text{lr}}$, with different energy scales, i.e.,

$$H_0 = (N_g + N_e - N_l)\delta + \sum_j \left(-\delta + \frac{U}{2} n^{(l)}_{j+1/2}\right)(n^{(l)}_{j+1/2} - 1), \tag{15}$$

where N_g and N_e are the total numbers of atoms in the g and e states, respectively, and N_l is the total number of links. From Eq. (15), it is immediate to see that for $\delta, U-\delta > 0$, the lowest-energy states of H_0 have exactly one atom (either g or e) on each half-integer site, i.e., $n^{(l)}_{j+1/2} = 1$ for every j: a double occupancy $n^{(l)}_{j+1/2} = 2$ costs energy $U - \delta$, while having a hole $n^{(l)}_{j+1/2} = 0$ costs energy δ. The term H_1 has the form

$$\begin{aligned} H_1 = &\sum_{j\ \text{odd}} \left[-t_g \left(c^\dagger_j c_{j+1/2} + c^\dagger_j c_{j-1/2} + \text{H.c.}\right) + \epsilon\, c^\dagger_j c_j\right] \\ &+ \sum_{j\ \text{even}} \left[-t_e \left(d^\dagger_j d_{j+1/2} + d^\dagger_j d_{j-1/2} + \text{H.c.}\right) - \epsilon\, d^\dagger_j d_j\right] \\ &+ H_D, \end{aligned} \tag{16}$$

where H_D is the Hamiltonian in Eq. (13).

We initialize the system with two g atoms for every g triple well and one e atom for every e triple well (all these quantities are locally conserved, if we neglect H_{lr}). The effective Hamiltonian describing the resonant dynamics is obtained using perturbation theory: we neglect H_{lr} and we treat H_1 as a perturbation to H_0. To second order, the effective Hamiltonian has the form (see Appendix B)

$$\begin{aligned} H^{(2)}_{\text{eff}} = &-w \sum_{j\ \text{odd}} (c^\dagger_j c_{j+1/2} d^\dagger_{j+1/2} d_{j+1} + \text{H.c}) \\ &- w \sum_{j\ \text{even}} (d^\dagger_j d_{j+1/2} c^\dagger_{j+1/2} c_{j+1} + \text{H.c}) \\ &+ m \sum_{j\ \text{odd}} c^\dagger_j c_j - m \sum_{j\ \text{even}} d^\dagger_j d_j, \end{aligned} \tag{17}$$

with

$$w = \frac{t_g t_e U}{\delta(\delta - U)} + \frac{-D_e t_g - D_g t_e + D_e D_g}{\delta - U}, \tag{18}$$

$$m = \epsilon + \frac{2t_g^2 - t_e^2}{2\delta} - \frac{(t_g - D_g)^2 - 2(t_e - D_e)^2}{2(U - \delta)}. \tag{19}$$

C. Mapping to the quantum link model

We now prove that there is an exact mapping between the effective Hamiltonian $H^{(2)}_{\text{eff}}$ and the quantum link Hamiltonian in Eq. (4). Note that in contrast to earlier works based on tilted 1D optical lattices [23–25], our goal here is to work within the lowest-energy manifold of the model.

The mapping is based on the following identification: sites having integer lattice positions $x = ja$, with $j \in \mathbb{Z}$, correspond to matter sites and, in particular, they can host positrons (for j even) or electrons (for j odd); half-integer lattice positions $x = (j + 1/2)a$, with $j \in \mathbb{Z}$ correspond to gauge field sites. More specifically, the fermionic operator ψ_j for the matter is defined as

$$\psi_j = \begin{cases} c_j, & j \text{ odd}, \\ d_j, & j \text{ even} \end{cases} \tag{20}$$

(and an analogous definition is used for $\psi^\dagger_j$). The electric field $E_{j,j+1}$ and the parallel transporter $U_{j,j+1}$ on the link are represented by

$$E_{j,j+1} = \frac{(-1)^j}{2}(c^\dagger_{j+1/2} c_{j+1/2} - d^\dagger_{j+1/2} d_{j+1/2}), \tag{21}$$

$$U_{j,j+1} = \begin{cases} c_{j+1/2} d^\dagger_{j+1/2}, & j \text{ odd}, \\ d_{j+1/2} c^\dagger_{j+1/2}, & j \text{ even} \end{cases} \tag{22}$$

and satisfy the desired commutation relation $[E_{i,i+1}, U_{j,j+1}] = \delta_{i,j}\, U_{j,j+1}$. With the definitions in Eqs. (20) and (21), the operator G_j takes the form

$$G_j = \frac{1}{2}(n^{(l)}_{j+1/2} + n^{(l)}_{j-1/2}) - n^{(b)}_j + \frac{(1 - (-1)^j)}{2}, \tag{23}$$

where $n^{(b)}_j$ is the number of atoms in the jth triple-well (or “block”), i.e.,

$$n^{(b)}_j = \begin{cases} c^\dagger_j c_j + c^\dagger_{j+1/2} c_{j+1/2} + c^\dagger_{j-1/2} c_{j-1/2}\ j \text{ odd}, \\ d^\dagger_j d_j + d^\dagger_{j+1/2} d_{j+1/2} + d^\dagger_{j-1/2} d_{j-1/2}\ j \text{ even}. \end{cases} \tag{24}$$

With this mapping, which is schematically shown in Fig. 1, we obtain that $H^{(2)}_{\text{eff}}$ is equivalent to the Hamiltonian H_{QLM} with $\tau = 0$, as can be readily obtained by substituting Eqs. (20)–(22) in Eq. (4). The gauge-invariant subspace corresponds to the sector with $n^{(l)}_{j+1/2} = 1$ and $n^{(b)}_j = [3 - (-1)^j]/2$ for every j: the first condition also implies that the electric field has ±1/2 as the only two possible eigenvalues and therefore corresponds to the spin-1/2 representation of the QLM model. Some examples of gauge-invariant states are shown in Fig. 4.

In Fig. 4(a), all g atoms sit on the links and all e atoms are on the matter sites: the corresponding electric field takes values $E_{j,j+1} = (-1)^j/2$, while $\psi^\dagger_j \psi_j = 1, 0$ for even and odd sites, respectively, leading to alternating positive and negative charges on matter sites. This state is the

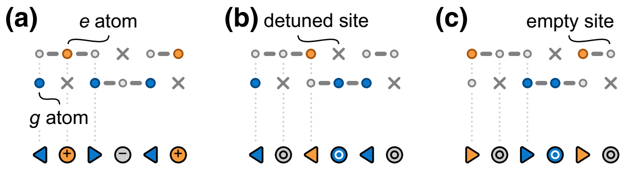

neighboring pairs of + and − charges

vacuum with negative electric field

vacuum with positive electric field

FIG. 4. Examples of the mapping between atomic configurations in the optical lattice and gauge-invariant states in the U(1) QLM. In each panel, the atomic states in the optical lattice are shown in the top row and the states in the QLM are shown in the bottom row. (a) The state with neighboring pairs of + and − charges. (b) The vacuum state with a homogeneous negative electric field $E = -1/2$. (c) The vacuum state with a homogeneous positive electric field $E = +1/2$.

ground state of the model in the limit $m \to -\infty$. Similarly, it is easy to show that the states represented in Figs. 4(b) and 4(c) have no charges on matter sites and have uniform (negative or positive) electric field. These states (*vacua*) are degenerate ground states in the limit $m \gg |w|$ with $\tau = 0$, while the degeneracy is split for $\tau \neq 0$.

D. Theta term

We now show how to tune the parameters of the optical lattice to obtain $\tau \neq 0$. The lattice Hamiltonian given in Eq. (9) is derived with the assumption that $\varphi = 0$. We now slightly perturb this model, by introducing a small shift $\varphi \ll 1$. To first order in φ, the shift produces an additional potential along x:

$$V_\alpha^x \to V_\alpha^x - A_\alpha \sin\left(\frac{\pi}{a}x\right)\varphi. \tag{25}$$

The main effect of this additional term is to change the chemical potential at half-integer positions $x = (j + 1/2)a$ by a quantity $-A_\alpha \varphi (-1)^j$. We obtain

$$\begin{aligned} H_{\text{latt}} \to H_{\text{latt}} &- \sum_j (-1)^j \varphi (A_g c^\dagger_{j+1/2} c_{j+1/2} \\ &+ A_e d^\dagger_{j+1/2} d_{j+1/2}) \\ = H_{\text{latt}} &- \sum_j (-1)^j \varphi \left[\frac{A_g + A_e}{2} n^{(l)}_{j+1/2} \right. \\ &+ \left. \frac{A_g - A_e}{2} (c^\dagger_{j+1/2} c_{j+1/2} - d^\dagger_{j+1/2} d_{j+1/2}) \right]. \end{aligned} \tag{26}$$

The term $\sum_j (-1)^j n^{(l)}_{j+1/2}$ cancels in the resonant sector and the remaining term is mapped to $\sum_j \tau E_{j,j+1}$, with

$$\tau = (A_e - A_g)\varphi. \tag{27}$$

Note that a similar scheme for the tuning of the topological theta angle has been proposed [46,47] for an experimental realization based on a tilted optical superlattice [23–25], which requires the implementation of an additional optical potential with twice the period of the superlattice.

IV. EXPERIMENTAL IMPLEMENTATION

The *ab initio* calculation of the band structure and Wannier functions allows us to estimate the energy scales involved in the quantum simulation. These estimations explicitly verify that the desired parameter range is achievable in present-day experiments. The quantitative estimation of the parameters is also crucial to understand the limitations of our proposal, such as the amplitude and duration of the signal, and to identify the main sources of error, such as the population of higher bands, higher-order perturbative processes, longer-range terms, and dissipation.

To set values, we choose the fermionic isotope ^{173}Yb with mass $M \approx 173u$ and the interorbital scattering length $a^-_{eg} = 219.7\ a_0$ [63]; here, u denotes the atomic mass unit and a_0 the Bohr radius. However, we note that our proposal can be similarly applied to other fermionic AELA species such as ^{171}Yb and ^{87}Sr. The experimental parameters require scaling to account for the modified atomic mass and scattering length [64,65] with no conceptual change in the design of the experiment.

A. Realistic parameters

We define $\Delta_{g/e}$ as the gap between the third and fourth energy band in the lattice for the g/e atoms (see Sec. A). The parameters used here are chosen to satisfy the hierarchy of energy scales

$$\Delta_{g/e} \gg \delta_{g/e}, U - \delta_{g/e} \gg t_{g/e}, D_{g/e} \gg \text{terms in } H_{\text{lr}}. \tag{28}$$

We note that for the 3D lattice potential $V_\alpha(\mathbf{r})$, the Wannier functions obtained by solving the noninteracting Hamiltonian H_{nonint} can be factorized in three directions. The hoppings t_α, the chemical potentials δ_α, and the gaps Δ_α do not depend on the y and z components $\phi^y_\alpha(y)$ and $\phi^z_\alpha(z)$ of the Wannier functions (see Appendix A). The interactions U and D_α, on the other hand, are proportional to the quantity

$$J_{yz} = \int dy\, dz\, |\phi^y_g(y)|^2 |\phi^y_e(y)|^2 |\phi^z_g(z)|^2 |\phi^z_e(z)|^2. \tag{29}$$

We can therefore tune F_α and $d_{y/z}$ to change the value of J_{yz} and thus enhance or suppress the interaction terms U and $D_{g/e}$ independent of the other parameters.

In Table I, we report a possible choice for the parameters of the optical lattice and the corresponding parameters of the lattice Hamiltonian. We choose $a = \lambda_{\text{m}} = 0.7594\ \mu\text{m}$ [66] and $J_{yz} = 48.566\ \mu\text{m}^{-2}$.

With these parameters, from Eqs. (18) and (19) we obtain $m/h = 9$ Hz and $w/h = -18$ Hz; where h denotes

Planck's constant. The value of J_{yz} reported here can be obtained with a transverse confinement $F_g/h = F_e/h =$ 48.9 kHz and $d_{y/z} = \lambda_m/2$. For this choice of transverse potential, the hopping in the y and z directions is $t_\alpha^{y/z}/h =$ 2 Hz, much smaller than the relevant scales m and w. The transverse hopping can be made even smaller by using two beams intersecting at a shallow angle instead of using retroreflected beams: the lattice spacing $d_{y/z}$ is increased and the same value of J_{yz} is obtained for a larger F_α, thus suppressing the transverse hopping.

We explicitly check that all the terms included in H_{lr}, which are neglected in the derivation of H_{QLM}, are small with respect to w. The nearest-neighbor density-density interaction is of the order of approximately 0.6 $h \times$ Hz, while the hopping between the sites $s = +$ and $s = -$ in a triple well is approximately 2 $h \times$ Hz and is negligible because it is suppressed by the on-site interaction U.

The parameters in Table I can be readily generalized to other atomic species: we can define the adimensional lattice constant $\tilde{a} = a/\lambda_m$ and the adimensional parameter $\tilde{A}_\alpha = A_\alpha 2M/\hbar^2\lambda_m^2$. Similarly, we can define dimensionless parameters for the other energy scales B_α, C_α, Δ_α, δ_α, U, t_α, D_α, m, and w and for the quantity J_{yz}. Implementations with different atomic species but the same adimensional parameters of the optical lattice yield the same adimensional values for the terms in the lattice Hamiltonian.

B. Initial-state preparation

We propose two distinct approaches to a two-step preparation of the system in gauge-invariant initial states as shown in Fig. 4, which require specific atom configurations. First, the correct atom-number distribution needs to be prepared (independent of the internal state). One option is to prepare it starting from a sample with one g atom per lattice site followed by the removal of atoms on selected lattice sites, yielding the desired occupation. This is a standard technique in quantum gas microscopes [67,68]. Alternatively, the atoms could be placed directly at their desired locations with moving optical-tweezer potentials [62]. In the second step, g atoms can be converted to e atoms on selected lattice sites using a global clock-laser excitation pulse exploiting the local differential light shifts δ_α and Δ_α [Fig. 1(a)]. The conversion could also be performed locally by using clock-laser light focused onto single lattice sites.

V. REAL-TIME DYNAMICS

Using numerical simulations, we study here the real-time dynamics of the model of the Hamiltonian given in Eq. (9), which we compare with the dynamics of the quantum link model in Eq. (4). In both cases, we start with the initial state shown in Fig. 4(a). The time evolution of the model is simulated exactly for a system of length $4a$ with periodic boundary conditions, with the parameters reported in Sec. IV A. Longer-range terms from H_{lr} in Eq. (9) are included in the numerical simulation: the dynamics are exact as long as higher bands are not occupied.

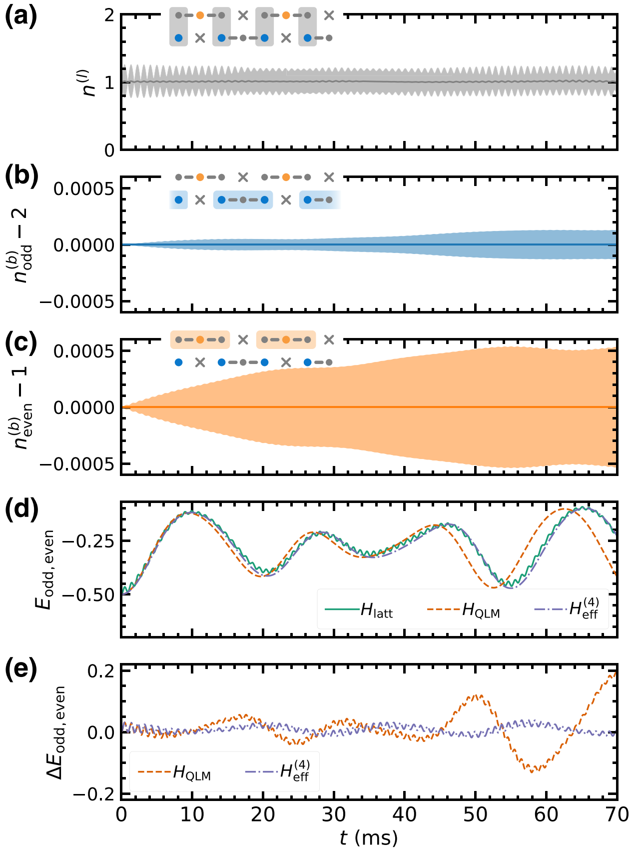

FIG. 5. The dynamics in the U(1) quantum link model. The time evolution of (a) the number of atoms per link and (b) [(c)] the number of atoms on each odd (even) block. For each observable O, the shaded area indicates the interval $\langle O\rangle \pm \sqrt{\mathrm{Var}(O)}$. The initial state is depicted in Fig. 4(a) and is evolved under H_{latt}. The system has periodic boundary conditions and finite size $4a$. The top-left schematic in each panel illustrates the observable. (d) The time evolution of the electric field on an odd-even link. The exact dynamics given by H_{latt} are compared with the second-order effective Hamiltonian [using Eqs. (18) and (19)] and with the fourth-order effective Hamiltonian $H^{(4)}_{\mathrm{eff}}$. The latter two are both equivalent to H_{QLM}. (e) The difference $\Delta E_{\mathrm{odd,even}} = \langle E_{\mathrm{odd,even}}\rangle_{H_{\mathrm{latt}}} - \langle E_{\mathrm{odd,even}}\rangle_H$ (the subscript denotes the Hamiltonian that generates the time evolution) for the two cases $H = H_{\mathrm{QLM}}$ and $H = H^{(4)}_{\mathrm{eff}}$.

A. Gauge invariance and gauge field

The system is effectively gauge invariant as long as Gauss's law applies. To quantify the violation of Gauss's law in Eq. (9), we examine the time evolution of $n^{(l)}_{j+1/2}$ and $n^{(b)}_j$. The simulation results are shown in Figs. 5(a)–5(c). We find that the conditions $n^{(b)}_j = [3 + (-1)^j]/2$ and

$n^{(l)}_{j+1/2} = 1$ are preserved up to 5×10^{-4} and 10^{-1}, respectively, within the first 70 ms after initialization, which should be compared to the characteristic interaction time scale $\hbar/|w| \simeq 8.8$ ms.

In Fig. 5(d), we examine the evolution of the electric field with (i) the Hamiltonian $H_{\rm latt}$, (ii) the second-order effective Hamiltonian $H^{(2)}_{\rm eff}$, equivalent to $H_{\rm QLM}$, and (iii) the fourth-order effective Hamiltonian $H^{(4)}_{\rm eff}$ (from the Schrieffer-Wolff procedure). The differences between the electric field value obtained in case (i) and with the approximate Hamiltonians are plotted in Fig. 5(e). For times up to approximately 40 ms, the results obtained in the three cases are in good agreement: this shows that the second-order effective Hamiltonian $H_{\rm QLM}$ captures the main features of the time evolution, at least at short and intermediate time scales, and that longer-range terms and higher-order perturbative processes are minor sources of error. For times of the order of $\gtrsim 50$ ms, we find that fourth-order corrections have to be considered in order to obtain a good prediction of the time evolution in the experiment. We remark that the fourth-order corrections do not violate Gauss's law but correspond to additional gauge-invariant terms. A feature of the evolution induced by $H_{\rm latt}$ that is not observed in the effective Hamiltonians is the presence of fast oscillations with small amplitude. These oscillations have a frequency compatible with the energy scale of H_0 and are averaged out in the perturbative approach.

To make this separation of energy scales more evident, we examine the Fourier transform of the signal $E(\omega) = \int_0^{t_{\rm max}} E(t)e^{-i\omega t}dt$ in Fig. 6. As expected, the evolution under $H_{\rm latt}$ shows peaks at frequency $\omega \sim \delta/\hbar = (U-\delta)/\hbar = 6.4$ kHz [Fig. 6(a)], which are not observed for the effective Hamiltonians. Enlarging at smaller frequencies [Fig. 6(b)], we see that the agreement in the Fourier transforms is good between $H_{\rm latt}$ and $H_{\rm QLM}$ and is excellent between $H_{\rm latt}$ and $H^{(4)}_{\rm eff}$.

B. Dissipation

Finite dissipation can become a crucial issue in the experiment when it occurs on time scales comparable to the relevant dynamic evolution of the system. Therefore, we focus on identifying the fastest dissipation process. This allows us to estimate for how long the experimental system closely follows the coherent dynamics of our model. For the AELA in an optical lattice considered here, the typically dominant dissipation channels are lossy collisions between pairs of atoms and off-resonant scattering of optical-lattice photons. In the following, we evaluate the relevance of both for our proposed experimental implementation.

Lossy collisions between pairs of atoms with one or both of the two atoms in the *e* state can lead to a particularly fast atom loss [48,49]. For our proposed implementation, however, double occupancies of lattice sites are (purposefully) strongly suppressed, either by fermionic quantum statistics (*ee* pairs) or a large on-site interaction energy (*eg* pairs). As a consequence, lossy collisions between pairs are not expected to be a limiting factor.

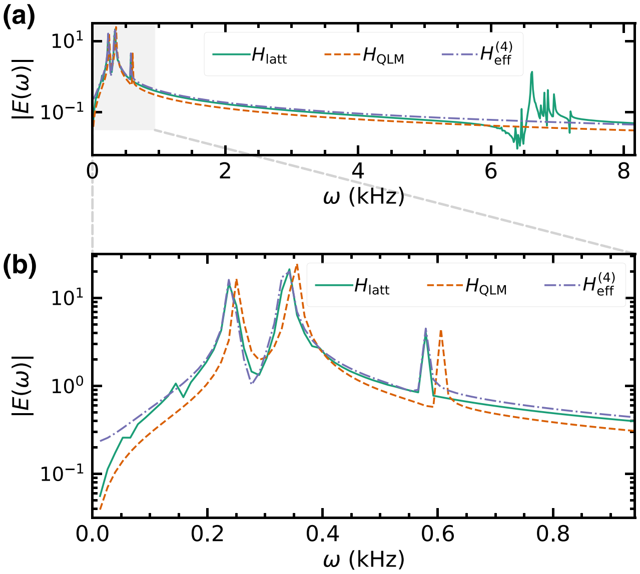

FIG. 6. The Fourier transform of the time evolution of the electric field. (a) The spectrum corresponding to the time evolution shown in Fig. 5(d). (b) An enlargement of (a), revealing details at small frequencies.

In contrast, off-resonant photon scattering from lattice photons is identified as the dominant limiting factor in our proposed implementation. While off-resonant photon scattering eventually leads to heating and atom loss, another effect could become relevant at earlier times. When an atom in the *e* state scatters an optical-lattice photon, short-lived intermediate states can be populated and decay back to the *g* state with a finite probability. Conversion of *e* atoms to *g* atoms due to this optical pumping process has already been observed and characterized in optical-lattice experiments with AELAs [35,69]. Here, we employ these results to estimate the expected time scale for our parameters (see Table I). Focusing on the proposed implementation in Sec. III A for ^{173}Yb and the off-resonant scattering of magic wavelength lattice light, we estimate a repumping rate $\Gamma \approx 111$ mHz. Comparison of this estimate to the quantity $|w|/\hbar = 113$ Hz suggests that the dynamics of our model can be faithfully observed for many characteristic time scales.

C. Disorder

An experimental implementation could also exhibit finite disorder. Based on previous experimental work [70], disorder occurs in particular when utilizing hybrid potentials generated with both optical lattices and optical tweezers. To estimate how much disorder affects the dynamic

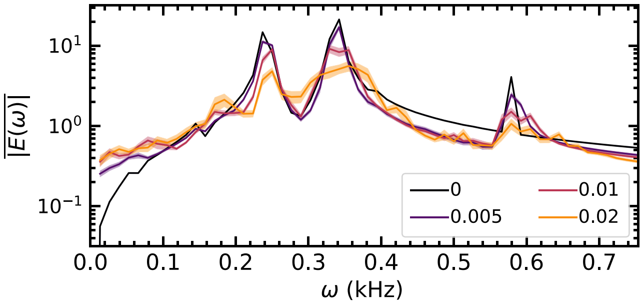

FIG. 7. The influence of disorder on the dynamics of the electric field. The Fourier transform of the time evolution of the electric field under H_W for different values of W. The legend indicates the values of W/h in kilohertz. The results are averaged over 100 disorder realizations.

evolution of the system, we consider a quenched disorder in the chemical potentials of the atoms of the form

$$\begin{aligned}H_W = H_{\text{latt}} &+ \sum_{j\text{ odd}} \Big[W_{g,j+1/2} c^{\dagger}_{j+1/2} c_{j+1/2} \\ &+ W_{g,j-1/2} c^{\dagger}_{j-1/2} c_{j-1/2} + W_j c^{\dagger}_j c_j \Big] \\ &+ \sum_{j\text{ even}} \Big[W_{e,j+1/2} d^{\dagger}_{j+1/2} d_{j+1/2} \\ &+ W_{e,j-1/2} d^{\dagger}_{j-1/2} d_{j-1/2} + W_j d^{\dagger}_j d_j \Big], \qquad (30)\end{aligned}$$

where $W_{\alpha,j+1/2}$ and W_j are taken randomly from a uniform distribution in the interval $[0, W)$.

In Fig. 7, we plot the Fourier transform $E(\omega)$ averaged over 100 disorder realizations for different values of W. We find that disorder has the effect of smearing out the peaks, which nevertheless remain visible up to $W/h \sim 0.01$ kHz.

VI. THE TWO-DIMENSIONAL MODEL

We now generalize the implementation examined in the previous sections to the quantum link model in two spatial dimensions and we show how this can be simulated with realistic experimental setups.

A. Quantum link model

We consider the following Hamiltonian that describes a two-dimensional (2D) quantum link model [71]:

$$\begin{aligned}H_{\text{QLM}} = &-w \sum_r \sum_{k=\hat{x},\hat{y}} \left(\psi^{\dagger}_r U_{r,r+k} \psi_{r+k} + \text{H.c.} \right) \\ &+ m \sum_r s_r \psi^{\dagger}_r \psi_r + \tau \sum_r \sum_{k=\hat{x},\hat{y}} E_{r,r+k}, \qquad (31)\end{aligned}$$

where the sums run over the points $r = (i,j)$ of a 2D square lattice (i,j are integers) and $s_r = (-1)^{i+j}$; here, $\hat{x}$ and $\hat{y}$ denote unit vectors along the respective directions. The gauge fields sit on the links and, similarly to the 1D case, are represented by spin variables with finite d-dimensional Hilbert spaces (here, $d = 2$). The generators of the gauge symmetry read

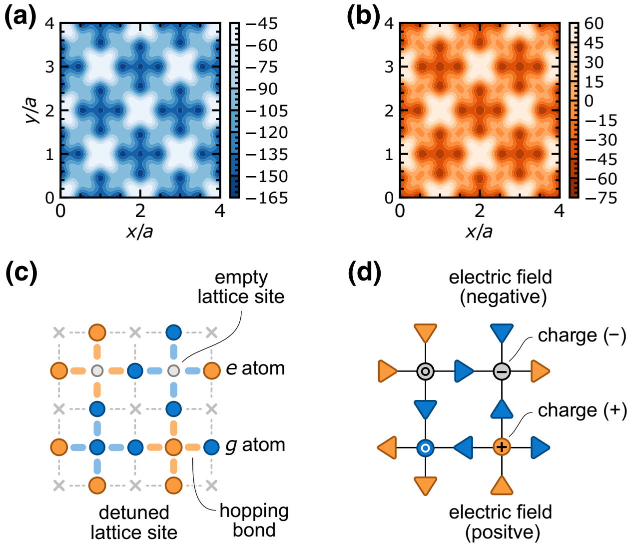

FIG. 8. The implementation of the quantum link model in two dimensions. (a),(b) The optical lattice for the (a) g and (b) e atoms. (c) An example of a gauge-invariant state belonging to the resonant subspace. The blue and orange circles represent g and e atoms, respectively. (d) The corresponding gauge-invariant state in the QLM. The dark- (light-) gray circles indicate the occupied (empty) matter sites (with charge +, −, or no charge). The red (blue) arrows represent a link with electric field $E_{r,r+k} = +1/2$ ($E_{r,r+k} = -1/2$).

$$G_r = \sum_{k=\hat{x},\hat{y}} (E_{r,r+k} - E_{r,r-k}) - \psi^{\dagger}_r \psi_r + \frac{1 - s_r}{2}. \qquad (32)$$

A state $|\Psi\rangle$ is gauge invariant in the vacuum symmetry sector without static charges if it satisfies Gauss's law $G_r |\Psi\rangle = 0$ for every lattice site r. An example of a gauge-invariant state is shown in Fig. 8(d).

Note that we do not include plaquette terms in Eq. (31), which are the most standard pure gauge-field terms. As we discuss below, the expected amplitudes of these terms would be too small in our proposed experimental setup to induce any notable change in the observed dynamics before off-resonant corrections break the gauge symmetry.

Note that different from the 1D case, in 2D QLMs, achieving the continuum limit is possible via dimensional reduction, via coupling several planes—similarly to what happens in CP(N) quantum field theories [72]. While this requires additional resources from an experimental standpoint, its implementation is compatible with all of the tools we discuss below.

TABLE II. The experimental parameters for the 2D quantum link model. All values are given in units of $h \times$ kHz.

$A_g = -A_e$	$B_g = B_e$	$C_g = C_e$
50.029	25.915	27.516

Δ	$\delta_g = \delta_e$	U	$t_g = t_e$	$D_g = D_e$
9.63	1.08	2.16	0.087	0.033

B. Quantum simulation

Our desired optical lattice in two dimensions consists of cross-shaped "blocks" of g and e sites [see Figs. 8(a)–8(c)]. While in the 1D case each block consists of a triple well, here a block contains five sites: a central matter site at $r = (x/a, y/a) = (i, j)$, with i, j integers, and four gauge sites around it at positions $r \pm (1/2, 0)$ and $r \pm (0, 1/2)$. Blocks of g and e sites alternate in a checkerboard pattern, as shown in Fig. 8(c), with overlapping g and e gauge sites. A lattice of this type can be realized with the potential

$$\begin{aligned} V_\alpha^{x,y}(x,y) = &- A_\alpha \sin^2\left[\frac{\pi}{2a}(x+y) + \varphi\right] - A_\alpha \sin^2\left[\frac{\pi}{2a}(x-y)\right] \\ &- B_\alpha \sin^2\left[\frac{\pi}{a}(x+y)\right] - B_\alpha \sin^2\left[\frac{\pi}{a}(x-y)\right] \\ &- C_\alpha \sin^2\left(\frac{2\pi}{a}x + \frac{\pi}{2}\right) - C_\alpha \sin^2\left(\frac{2\pi}{a}y + \frac{\pi}{2}\right). \end{aligned} \tag{33}$$

Figures 8(a) and 8(b) depicts the profiles of $V_g^{x,y}$ and $V_e^{x,y}$ for the values of A_g, A_e, B_g, B_e, C_g, and C_e reported in Table II.

The steps for deriving the lattice Hamiltonian and mapping it to the QLM are analogous to the 1D case. We report here the mapping of the operators:

$$E_{r,r+k} = \frac{s_r}{2}(c^\dagger_{r+k/2}c_{r+k/2} - d^\dagger_{r+k/2}d_{r+k/2}), \tag{34}$$

$$\psi_r = \begin{cases} c_r, & \text{if } s_r = -1, \\ d_r, & \text{if } s_r = +1, \end{cases} \tag{35}$$

$$U_{r,r+k} = \begin{cases} c_{r+k/2}d^\dagger_{r+k/2}, & \text{if } s_r = +1, \\ d_{r+k/2}c^\dagger_{r+k/2}, & \text{if } s_r = -1. \end{cases} \tag{36}$$

The system is initialized with three g atoms on each odd block and two e atoms on each even block. To illustrate the mapping, we show in Figs. 8(c) and 8(d) an example of a resonant state in the local-occupation basis and the corresponding gauge-invariant state in the quantum link model.

Using the same derivation as the 1D case, we obtain the effective Hamiltonian in Eq. (31). In Table II, we report the parameters obtained for the lattice potential depicted in Figs. 8(a) and 8(b). We set $a = \lambda_m = 0.7594$ µm and $J_z \equiv \int dz |\phi_g^z(z)|^2 |\phi_e^z(z)|^2 = 19.235$ µm^{-1}. For this choice of parameters, we obtain $m = 10$ $h \times$ Hz and $w = 20$ $h \times$ Hz for the QLM Hamiltonian Eq. (31).

We remark that plaquette terms of the form $U_{r,r+\hat{x}}\, U_{r+\hat{x},r+\hat{x}+\hat{y}}\, U^\dagger_{r+\hat{y},r+\hat{x}+\hat{y}}\, U^\dagger_{r,r+\hat{y}}$ are generated at higher order in perturbation theory but their amplitude is completely negligible for the energy scales of the experimental system. While it remains an open question whether plaquette terms can be implemented in a realistic experiment with similar setups, we note that in recent works it has been observed that some phases of matter that are expected to be stabilized by plaquette terms are surprisingly robust even when these terms are absent or completely negligible [22,73–75]. This suggests interesting directions for future investigation of static and dynamical properties of LGTs with no plaquette terms, such as the one in Eq. (31).

VII. CONCLUSIONS

We present a proposal for the scalable quantum simulation of lattice gauge theories coupling (staggered) fermions to U(1) gauge fields utilizing a mixture of alkaline-earth(-like) atoms in both a ground and a metastable state in optical potentials. The key element of our proposal is a careful treatment of the full system dynamics, which are derived *ab initio* from microscopic interactions between atoms and light, and the atoms themselves. While the proposal can be applied to a variety of atomic species, we draw a complete blueprint utilizing concrete estimates based on ^{173}Yb atoms.

Our treatment highlights concrete challenges in the quantum simulation of lattice gauge theories that have so far mostly been overlooked. In particular, it makes clear that the superposition of lattice potentials required for such simulations, while certainly realistic experimentwise, gives rise to complicated band structures that must be quantitatively understood to access the reliability and feasibility of any quantum simulation. The reason for this is twofold: band separation can become much smaller than what is naively expected, making protection of gauge invariance very challenging; in parallel, intrinsic energy scales of desired processes can be considerably reduced with respect to simplistic deep-lattice estimates based on highly localized Wannier functions. These limitations are particularly pernicious for single-body terms in the lattice potential, the estimation of which crucially requires a quantitative approach such as the one adopted here.

Within the context of our proposal, we show that optimal parameter regimes can still be found for observing the correct and expected LGT dynamics. This can be achieved due to the detailed microscopic understanding toward which our treatment leads. We demonstrate this conclusion by comparing numerical simulations of both ideal and effective dynamics of string relaxation, also including the effects of inhomogeneities.

Based on our findings, we believe that the *ab initio* approach that we propose is, in the long term, the one needed to fully determine the capabilities of quantum simulators of lattice gauge theories. We take the first step beyond Abelian 1D models, by extending them to 2D geometries. Future works will be fundamental to address the experimental capabilities to realize other Abelian gauge theories (such as QLMs with larger representations—or LGTs that do not belong to the class of QLMs, such as the conventional Wilsonian LGTs) and non-Abelian lattice gauge theories, which to date have been proposed only in very few settings [76–84].

ACKNOWLEDGMENTS

We thank M. Burrello, G. Pagano, and E. Rico for insightful discussions, and F. Scazza for collaboration on a related work. The work of M.D., P.F., and F.S. was partly supported by the European Research Council (ERC) under Grant No. 758329, “Atomic Gauge and Entanglement Theories” (AGEnTh), and by the Ministry of Education, University and Research (MIUR) Program FARE (Entanglement di sistemi a molticorpi in sistemi quantistici programmabili). M.A. and N.D.O. acknowledge funding from the Deutsche Forschungsgemeinschaft (DFG, German Research Foundation) under Germany’s Excellence Strategy—EXC-2111—390814868, from the ERC under the European Union Horizon 2020 research and innovation program (Grant Agreement No. 803047), and from the German Federal Ministry of Education and Research via the funding program “Quantum Technologies—from Basic Research To Market” (Contract No. 13N15895 FermiQP). M.A. and M.D. further acknowledge funding within the QuantERA II Program, which has received funding from the European Union Horizon 2020 research and innovation program under Grant Agreement No. 101017733.

APPENDIX A: WANNIER FUNCTIONS AND LATTICE HAMILTONIAN

1. 1D case

In this appendix, we discuss the *ab initio* derivation of the lattice Hamiltonian from the Wannier functions for the case of the 1D model. First, we solve the noninteracting Hamiltonian $H_{\rm nonint}$. We diagonalize the single-particle Hamiltonian $h_\alpha(\mathbf{r})$,

$$h_\alpha(\mathbf{r}) = -\frac{\hbar^2}{2M}\nabla^2 + V_\alpha(\mathbf{r}), \tag{A1}$$

with $\alpha = g, e$. For the quantum simulation of the 1D model discussed in Sec. III, the potential is

$$V_\alpha(\mathbf{r}) = V_\alpha^x(x) + V_\alpha^y(y) + V_\alpha^z(z). \tag{A2}$$

We then look for a factorized and localized 3D complete basis of wave functions for all states involved in the dynamic evolution of the system. The potential is periodic in space for each component x, y, and z such that the Bloch theorem applies to Eq. (A1). In Fig. 9, we plot the potential V_g^x (with the parameters of Table I) and the lowest bands obtained by solving the corresponding periodic Hamiltonian. Using a unitary transformation (similar to the reverse Fourier transformation) of the Bloch eigenfunctions, we obtain a set of localized orthonormal wave functions $w_{\alpha,s}$ called the Wannier functions. Because of the form of the potential in Eq. (A2), the Bloch functions are factorizable. Likewise, the Wannier functions factorize along x, y, and z:

$$w_{\alpha,s}(\mathbf{r}-\mathbf{r}_j) = \phi_{\alpha,s}^x(x-ja)\phi_\alpha^y(y)\phi_\alpha^z(z), \tag{A3}$$

where w is the 3D Wannier function and the ϕ^i are the 1D Wannier functions for each direction $i = x, y, z$. $\alpha = g, e$ is the electronic state, $s = \{0, +, -\}$ denotes the three functions corresponding to the three sites of a triple well, and $\mathbf{r}_j = ja\hat{x}$ is the Wannier center. As we target a 1D system, we consider only Wannier functions in the transverse directions y and z centered around $y = z = 0$ by convention. They involve only the lowest Bloch band. The x component is instead obtained from the three lowest bands such that we have three Wannier centers per unit cell.

To derive an expression for the localized Wannier functions that is useful to estimate the overlap, we compute the eigenstates of the projection of the position operator onto a given set of Bloch states [85,86]. In one dimension, this method always gives the maximally localized Wannier functions [87,88]. In many other cases, this derivation still gives a good approximation of the maximally localized Wannier functions.

We can then define discrete operators for the discrete Hamiltonian. We expand the fermionic operators in the basis of the Wannier functions

$$\begin{aligned}\Psi_g(\mathbf{r}) = \sum_{j\ \rm odd}\big[&w_{g,+}(\mathbf{r}-\mathbf{r}_j)c_{j+1/2}\\ &+w_{g,0}(\mathbf{r}-\mathbf{r}_j)c_j + w_{g,-}(\mathbf{r}-\mathbf{r}_j)c_{j-1/2}\big],\end{aligned} \tag{A4}$$

$$\begin{aligned}\Psi_e(\mathbf{r}) = \sum_{j\ \rm even}\big[&w_{e,+}(\mathbf{r}-\mathbf{r}_j)d_{j+1/2}\\ &+w_{e,0}(\mathbf{r}-\mathbf{r}_j)d_j + w_{e,-}(\mathbf{r}-\mathbf{r}_j)d_{j-1/2}\big].\end{aligned} \tag{A5}$$

We stress that the only approximations performed so far are (i) neglecting the higher bands and (ii) only considering the chain localized at $y, z = 0$. Approximation (i) is justified when the gaps Δ_g and Δ_e between the third and the closest higher bands (see Fig. 9) are much larger than the energy scales of the dynamics in which we are interested. Approximation (ii) is justified if the transverse hoppings t_α^y

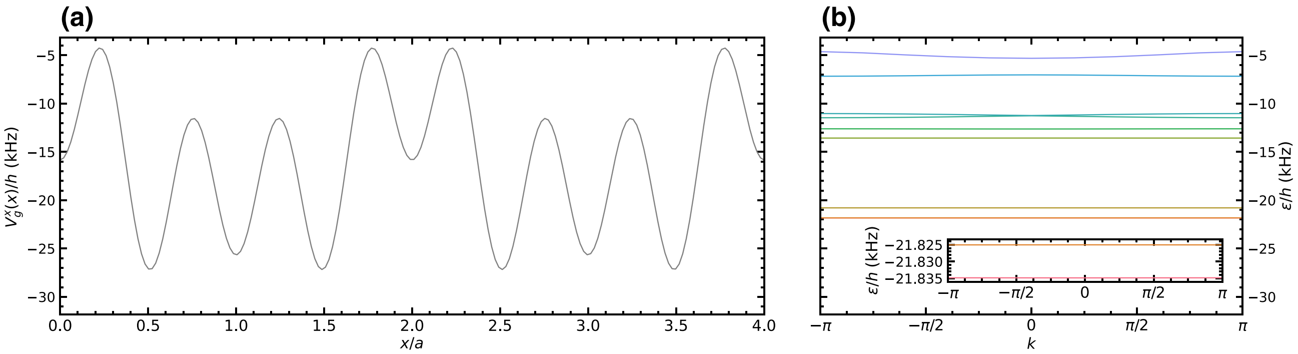

FIG. 9. The lattice potential and band structure along x. (a) The x component of the optical-lattice potential $V_g^x(x)$. The defining parameters are reported in Table I. (b) The corresponding band structure, using the same scale as in (a). The two lowest bands are almost degenerate (they correspond to symmetric and antisymmetric superpositions of the $s = \{+, -\}$ sites in the triple well) and are separated from the third one (corresponding to the central site 0 of the triple well) by an energy of approximately δ_g. Higher bands are separated from the first three by an energy gap Δ_g.

and t_α^z are small compared to the energy scales of our interest. For the gaps and the transverse hoppings of Sec. IV A, both approximations are appropriate.

The discrete parameters emerge when substituting Eqs. (A4) and (A5) in the Hamiltonian $H = H_{\text{nonint}} + H_{\text{int}}$ in Eq. (5). These parameters include the chemical potentials, the hoppings (both from H_{nonint}), the on-site and off-site density-density interactions, the density-mediated hoppings, and the correlated hoppings between g and e atoms. We include all these terms in the numerical simulations of the real-time dynamics in Sec. V. For clarity, we give the lattice Hamiltonian with the terms of highest amplitude. We define the chemical potentials such that

$$\begin{aligned}\mu_{\alpha,s} &= \int d^3\mathbf{r}\; w_{\alpha,s}^*(\mathbf{r} - \mathbf{r}_\alpha) h_\alpha(\mathbf{r}) w_{\alpha,s}(\mathbf{r} - \mathbf{r}_\alpha)\\ &= \mu_{\alpha,s}^x + \mu_\alpha^y + \mu_\alpha^z,\end{aligned} \tag{A6}$$

where $\alpha = g, e$, $s = \{0, +, -\}$, and the Wannier centers are $\mathbf{r}_g = a\hat{x}$ and $\mathbf{r}_e = 0$. We further define the difference between the chemical potentials in each triple well,

$$\delta_{\alpha,\pm} = \mu_{\alpha,0} - \mu_{\alpha,\pm} = \mu_{\alpha,0}^x - \mu_{\alpha,\pm}^x, \tag{A7}$$

and the nearest-neighbor hoppings within a triple well,

$$\begin{aligned}t_{\alpha,\pm} &= -\int d^3\mathbf{r}\; w_{\alpha,0}^*(\mathbf{r} - \mathbf{r}_\alpha) h_\alpha(\mathbf{r}) w_{\alpha,\pm}(\mathbf{r} - \mathbf{r}_\alpha)\\ &= -\int dx\; [\phi_{\alpha,0}^x(x - ja)]^* h_\alpha^x(x) \phi_{\alpha,\pm}^x(x - ja).\end{aligned} \tag{A8}$$

For $\varphi = 0$, the triple well is designed to be symmetrical, such that $\delta_{\alpha,+} = \delta_{\alpha,-} = \delta_\alpha$ and $t_{\alpha,+} = t_{\alpha,-} = t_\alpha$. These two terms result in the Hamiltonian terms H_g and H_e in Eq. (9).

The term with largest amplitude obtained from H_{int} is the on-site interaction on the sites where g and e triple wells overlap. This amplitude is given by

$$\begin{aligned}U &= g_{eg}^- \int d^3\mathbf{r}\; |w_{g,-}(\mathbf{r} - a\hat{x})|^2 |w_{e,+}(\mathbf{r})|^2\\ &= g_{eg}^- J_{yz} \int dx\; |\phi_{g,-}^x(x - ja)|^2 |\phi_{e,+}^x(x)|^2,\end{aligned} \tag{A9}$$

with

$$J_{yz} = \int dy\, dz\; |\phi_g^y(y)|^2 |\phi_e^y(y)|^2 |\phi_g^z(z)|^2 |\phi_e^z(z)|^2, \tag{A10}$$

and yields the Hamiltonian term H_U in Eq. (9). The terms with the next-largest amplitude with our choice of parameters are density-assisted hoppings; specifically, where a g or e atom hops between two sites of a triple well, provided that an atom of the opposite electronic state sits in either the initial or the final site (see Fig. 3). The amplitude has the form

$$\begin{aligned}D_g &= g_{eg}^- \int d^3\mathbf{r}\; w_{g,0}^*(\mathbf{r} - a\hat{x}) w_{g,-}(\mathbf{r} - a) |w_{e,+}(\mathbf{r})|^2\\ &= g_{eg}^- J_{yz} \int dx\; [\phi_{g,0}^x(x - ja)]^* \phi_{g,-}^x(x - ja) |\phi_{e,+}^x(x)|^2,\end{aligned} \tag{A11}$$

$$\begin{aligned}D_e &= g_{eg}^- \int d^3\mathbf{r}\; |w_{g,-}(\mathbf{r} - a\hat{x})|^2 w_{e,0}^*(\mathbf{r}) w_{e,+}(\mathbf{r}),\\ &= g_{eg}^- J_{yz} \int dx\; |\phi_{g,-}^x(x - ja)|^2 [\phi_{e,0}^x(x)]^* \phi_{e,+}^x(x)\end{aligned} \tag{A12}$$

and results in the Hamiltonian H_D in Eq. (9). For our choice of parameters, all the other terms (that we generically include in H_{lr}) have sufficiently small amplitudes to be negligible according to Sec. V A.

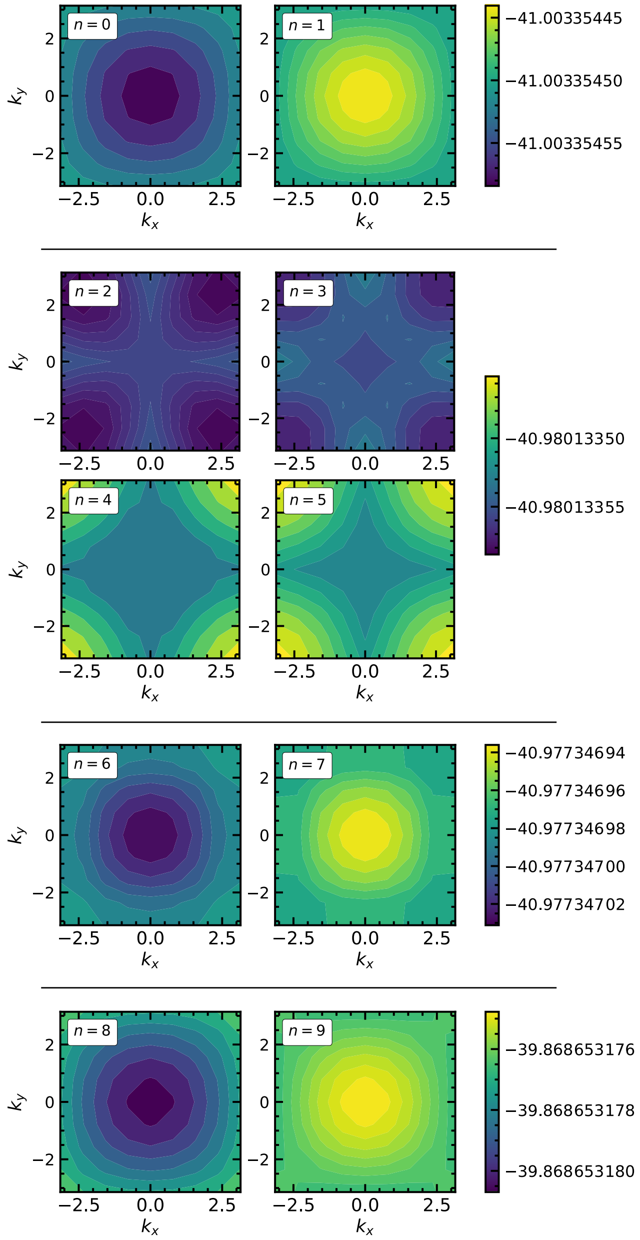

FIG. 10. The band structure for the 2D lattice. The ten lowest bands corresponding to the 2D lattice $V_e^{x,y}(x,y)$ in Fig. 8.

2. 2D case

The steps of the derivation of the lattice Hamiltonian in the 2D system are very similar to those for the 1D case. The main difference lies in the potential, which is now

$$V_\alpha(\mathbf{r}) = V_\alpha^{x,y}(x,y) + V_\alpha^z(z). \tag{A13}$$

As a consequence, only the z component of the Bloch (and Wannier) functions can be factorized out, while for the x-y plane we have to solve a 2D single-particle Hamiltonian. The first ten 2D Bloch bands for the parameters in Table II are plotted in Fig. 10.

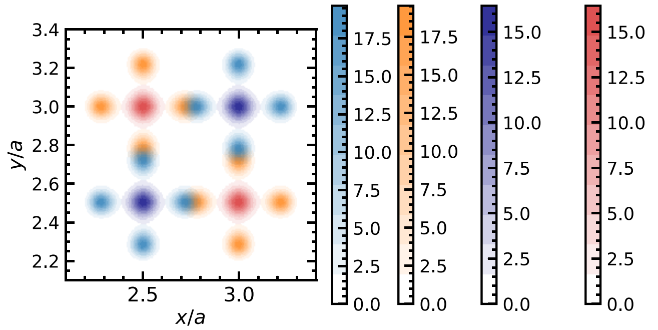

FIG. 11. The Wannier functions for the 2D lattice. The 2D Wannier functions of two g and two e blocks. In orange (light blue), we plot the four Wannier functions localized on the links of each block for the e (g) state. In red (dark blue), we plot the Wannier function localized on the center of each block for the e (g) state.

The unit cell that we consider is defined by the lattice vectors $(2a, 0)$ and $(0, 2a)$ and contains two blocks for each electronic state. Because each block contains five sites, we need ten Wannier functions per unit cell for each state. To find the Wannier functions, we first find the eigenstates of the projection of the x-position operator on the ten lowest bands: we collect the groups of eigenstates with (almost) degenerate eigenvalue and diagonalize the y-position operator projected on each group. The Wannier functions obtained with this procedure are plotted in Fig. 11. The coefficients of the lattice Hamiltonian are then obtained as in the 1D case.

APPENDIX B: PERTURBATIVE THEORY OF THE LATTICE HAMILTONIAN

The Hamiltonian given in Eq. (5), describing the cold atoms in the optical lattice, and its lattice formulation in Eq. (9) can be mapped to the QLM Hamiltonian in Eq. (4) when considering the coupling between the targeted gauge-invariant Hilbert subspace and the rest of the Hilbert space as a perturbation. Such a regime occurs when the three parameters ϵ, t_α, and D_α are small compared to both δ and $U - \delta$ and $H_{\rm lr}$ is negligible. To second order in perturbation, we obtain the correction given in Eq. (17). Here, we present the computation in more detail.

The resonant targeted subspace verifies that

$$\forall j \text{ even}, \qquad n^g_{j-1/2} + n^g_j + n^g_{j+1/2} = 2, \tag{B1}$$

$$\forall j \text{ odd}, \qquad n^e_{j-1/2} + n^e_j + n^e_{j+1/2} = 1, \tag{B2}$$

$$\forall j, \qquad n^e_{j+1/2} + n^g_{j+1/2} = 1, \tag{B3}$$

which satisfy the gauge-invariant condition $G_i|\psi\rangle = 0$ for all sites i and $|\psi\rangle$ in the targeted subspace. All states within this targeted subspace have the same energy relative to the Hamiltonian H_0 in Eq. (15), although they are not its

TABLE III. A couple of processes (arrows) starting and ending with a gauge-invariant state (full color) are illustrated. The transparent dots correspond to the intermediate state. First-order corrections to the energy are neglected in the amplitude of each process. $m = (\delta_e - \delta_g)/2$.

Processes	Amplitude	Add to
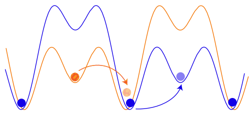	$-\frac{t_g t_e U}{\delta(U-\delta)} - \frac{D_e t_g}{U-\delta}$ $-\frac{D_g t_e}{U-\delta} - \frac{D_e D_g}{U-\delta}$	w
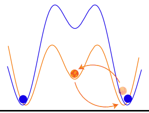	$-\frac{t_e^2}{U-\delta}$ $-2\frac{t_e D_e}{U-\delta} - \frac{D_e^2}{U-\delta}$	δ_e (x2)
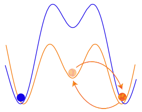	$-\frac{t_e^2}{\delta}$	δ_e
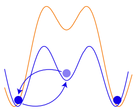	$-\frac{t_g^2}{\delta}$	δ_g (x2)
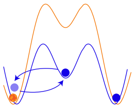	$-\frac{t_g^2}{U-\delta}$ $-2\frac{t_g D_g}{U-\delta} - \frac{D_g^2}{U-\delta}$	δ_g

ground states. This subspace is separated from all other orthogonal states coupled by H_1 in Eq. (16) by an energy proportional to δ and U. It is thus possible to apply standard quantum perturbation theory by treating H_1 as a perturbation to H_0 with ratios of t_α and D_α, with $1/\delta$ or $1/(U-\delta)$ as the small parameters. To first order, the terms in ϵ of H_1 generate a contribution in the staggered mass m. Further corrections due to these terms are negligible and are neglected. The eigenfunctions of the resonant subspace in the Fock basis are not modified to first order.

To find Eq. (17), we continue the perturbation to second order. We use the perturbation formula

$$H_{\text{eff}}^{(2)} = \sum_{i,j}\sum_{\phi} \frac{|\psi_i\rangle\langle\psi_i|H_1|\phi\rangle\langle\phi|H_1|\psi_j\rangle\langle\psi_j|}{E_\phi - E_\psi}, \tag{B4}$$

with $H_0|\psi_i\rangle = E_\psi|\psi_i\rangle$, for all i where the ψ_i generate the resonant subspace, and the ϕ are all states orthogonal to the ψ_i such that $\langle\psi_i|H_1|\phi\rangle \neq 0$. By definition, we take $H_0|\phi\rangle = E_\phi|\phi\rangle$. Both sets of states $\{|\psi_i\rangle\}$ and $\{|\phi\rangle\}$ are separable in the local Fock basis and H_1 is short ranged such that, in Eq. (B4), we may only consider a couple of processes (i.e., matrix elements of $\langle\psi_i|H_1|\phi\rangle\langle\phi|H_1|\psi_j\rangle$) involving one link or one site. All of these processes, their amplitude, and the amplitude to which they contribute are listed in Table III.

[1] K. G. Wilson, Confinement of quarks, Phys. Rev. D **10**, 2445 (1974).

[2] J. B. Kogut, An introduction to lattice gauge theory and spin systems, Rev. Mod. Phys. **51**, 659 (1979).

[3] I. Montvay and G. Muenster, *Quantum Fields on a Lattice* (Cambridge University Press, Cambridge, United Kingdom, 1994).

[4] Z. Fodor and C. Hoelbling, Light hadron masses from lattice QCD, Rev. Mod. Phys. **84**, 449 (2012).

[5] W. Detmold, R. G. Edwards, J. J. Dudek, M. Engelhardt, H.-W. Lin, S. Meinel, K. Orginos, and P. Shanahan, Hadrons and nuclei, Eur. Phys. J. A **55**, 1 (2019).

[6] C. DeTar and U. Heller, QCD thermodynamics from the lattice, Eur. Phys. J. A **41**, 405 (2009).

[7] K. Fukushima and T. Hatsuda, The phase diagram of dense QCD, Rep. Prog. Phys. **74**, 014001 (2010).

[8] O. Philipsen, Constraining the QCD phase diagram at finite temperature and density (2019), ArXiv:1912.04827.

[9] S. Borsanyi, Z. Fodor, J. Guenther, C. Hoelbling, S. Katz, L. Lellouch, T. Lippert, K. Miura, L. Parato, and K. Szabo, *et al.*, Leading hadronic contribution to the muon magnetic moment from lattice QCD, Nature **593**, 51 (2021).

[10] U. J. Wiese, Ultracold quantum gases and lattice systems: Quantum simulation of lattice gauge theories, Ann. Phys. **525**, 777 (2013).

[11] M. Dalmonte and S. Montangero, Lattice gauge theories simulations in the quantum information era, Contemp. Phys. **57**, 388 (2016).

[12] E. Zohar, I. Cirac, and B. Reznik, Quantum simulations of lattice gauge theories using ultracold atoms in optical lattices, Rep. Prog. Phys. **79**, 014401 (2016).

[13] M. C. Bañuls, R. Blatt, J. Catani, A. Celi, J. I. Cirac, M. Dalmonte, L. Fallani, K. Jansen, M. Lewenstein, and S. Montangero, *et al.*, Simulating lattice gauge theories within quantum technologies, Eur. Phys. J. D **74**, 1 (2020).

[14] M. Aidelsburger, L. Barbiero, A. Bermudez, T. Chanda, A. Dauphin, D. González-Cuadra, P. R. Grzybowski, S. Hands, F. Jendrzejewski, and J. Jünemann, *et al.*, Cold atoms meet lattice gauge theory, Phil. Trans. R. Soc. A. **380**, 20210064 (2022).

[15] Z. Davoudi, C. Bauer, A. Balantekin, T. Bhattacharya, M. Carena, W. A. de Jong, P. Draper, A. El-Khadra, N. Gemelke, and M. Hanada, *et al.*, Quantum simulation for high energy physics (2022), ArXiv:2204.03381.

[16] E. A. Martinez, C. A. Muschik, P. Schindler, D. Nigg, A. Erhard, M. Heyl, P. Hauke, M. Dalmonte, T. Monz, P. Zoller, and R. Blatt, Real-time dynamics of lattice gauge theories with a few-qubit quantum computer, Nature **534**, 516 (2016).

[17] N. H. Nguyen, M. C. Tran, Y. Zhu, A. M. Green, C. H. Alderete, Z. Davoudi, and N. M. Linke, Digital quantum simulation of the Schwinger model and symmetry protection with trapped ions (2021), ArXiv:2112.14262.

[18] C. Schweizer, F. Grusdt, M. Berngruber, L. Barbiero, E. Demler, N. Goldman, I. Bloch, and M. Aidelsburger, Floquet approach to $\mathbb{Z}_2$ lattice gauge theories with ultracold atoms in optical lattices, Nat. Phys. **15**, 1168 (2019).

[19] A. Mil, T. V. Zache, A. Hegde, A. Xia, R. P. Bhatt, M. K. Oberthaler, P. Hauke, J. Berges, and F. Jendrzejewski, A scalable realization of local U(1) gauge invariance in cold atomic mixtures, Science **367**, 1128 (2020).

[20] H. Bernien, S. Schwartz, A. Keesling, H. Levine, A. Omran, H. Pichler, S. Choi, A. S. Zibrov, M. Endres, and M. Greiner, *et al.*, Probing many-body dynamics on a 51-atom quantum simulator, Nature **551**, 579 (2017).

[21] F. M. Surace, P. P. Mazza, G. Giudici, A. Lerose, A. Gambassi, and M. Dalmonte, Lattice Gauge Theories and String Dynamics in Rydberg Atom Quantum Simulators, Phys. Rev. X **10**, 021041 (2020).

[22] G. Semeghini, H. Levine, A. Keesling, S. Ebadi, T. T. Wang, D. Bluvstein, R. Verresen, H. Pichler, M. Kalinowski, and R. Samajdar, *et al.*, Probing topological spin liquids on a programmable quantum simulator, Science **374**, 1242 (2021).

[23] B. Yang, H. Sun, R. Ott, H.-Y. Wang, T. V. Zache, J. C. Halimeh, Z.-S. Yuan, P. Hauke, and J.-W. Pan, Observation of gauge invariance in a 71-site Bose-Hubbard quantum simulator, Nature **587**, 392 (2020).

[24] Z.-Y. Zhou, G.-X. Su, J. C. Halimeh, R. Ott, H. Sun, P. Hauke, B. Yang, Z.-S. Yuan, J. Berges, and J.-W. Pan, Thermalization dynamics of a gauge theory on a quantum simulator, Science **377**, 311 (2022).

[25] H.-Y. Wang, W.-Y. Zhang, Z.-Y. Yao, Y. Liu, Z.-H. Zhu, Y.-G. Zheng, X.-K. Wang, H. Zhai, Z.-S. Yuan, and J.-W. Pan, Interrelated thermalization and quantum criticality in a lattice gauge simulator (2022), ArXiv:2210.17032.

[26] A. Frölian, C. S. Chisholm, E. Neri, C. R. Cabrera, R. Ramos, A. Celi, and L. Tarruell, Realizing a 1D topological gauge theory in an optically dressed BEC, Nature **608**, 293 (2022).

[27] E. Zohar, Quantum simulation of lattice gauge theories in more than one space dimension—requirements, challenges and methods, Phil. Trans. R. Soc. A. **380**, 20210069 (2022).

[28] Y. Y. Atas, J. Zhang, R. Lewis, A. Jahanpour, J. F. Haase, and C. A. Muschik, SU(2) hadrons on a quantum computer via a variational approach, Nat. Commun. **12**, 6499 (2021).

[29] Y. Y. Atas, J. F. Haase, J. Zhang, V. Wei, S. M.-L. Pfaendler, R. Lewis, and C. A. Muschik, Simulating one-dimensional quantum chromodynamics on a quantum computer: Real-time evolutions of tetra- and pentaquarks (2022), ArXiv:2207.03473.

[30] G. Pardo, T. Greenberg, A. Fortinsky, N. Katz, and E. Zohar, Resource-efficient quantum simulation of lattice gauge theories in arbitrary dimensions: Solving for Gauss' law and fermion elimination (2022), ArXiv:2206.00685.

[31] R. Irmejs, M. C. Banuls, and J. I. Cirac, Quantum simulation of Z2 lattice gauge theory with minimal requirements (2022), ArXiv:2206.08909.

[32] E. Zohar and J. I. Cirac, Removing staggered fermionic matter in $U(N)$ and $SU(N)$ lattice gauge theories, Phys. Rev. D **99**, 114511 (2019).

[33] J. Osborne, I. P. McCulloch, B. Yang, P. Hauke, and J. C. Halimeh, Large-scale $2+1D$ U(1) gauge theory with dynamical matter in a cold-atom quantum simulator (2022), ArXiv:2211.01380.

[34] J. C. Halimeh, L. Homeier, C. Schweizer, M. Aidelsburger, P. Hauke, and F. Grusdt, Stabilizing lattice gauge theories through simplified local pseudogenerators, Phys. Rev. Res. **4**, 033120 (2022).

[35] L. Riegger, N. Darkwah Oppong, M. Höfer, D. R. Fernandes, I. Bloch, and S. Fölling, Localized Magnetic Moments with Tunable Spin Exchange in a Gas of Ultracold Fermions, Phys. Rev. Lett. **120**, 143601 (2018).

[36] A. Heinz, A. J. Park, N. Šantić, J. Trautmann, S. G. Porsev, M. S. Safronova, I. Bloch, and S. Blatt, State-Dependent Optical Lattices for the Strontium Optical Qubit, Phys. Rev. Lett. **124**, 203201 (2020).

[37] J. Schwinger, On gauge invariance and vacuum polarization, Phys. Rev. **82**, 664 (1951).

[38] E. A. Calzetta and B. L. Hu, *Nonequilibrium Quantum Field Theory* (Cambridge University Press, Cambridge, United Kingdom, 2008).

[39] J. Kogut and L. Susskind, Hamiltonian formulation of Wilson's lattice gauge theories, Phys. Rev. D **11**, 395 (1975).

[40] L. Susskind, Lattice fermions, Phys. Rev. D **16**, 3031 (1977).

[41] D. Horn, Finite matrix models with continuous local gauge invariance, Phys. Lett. B **100**, 149 (1981).

[42] P. Orland and D. Rohrlich, Lattice gauge magnets: Local isospin from spin, Nucl. Phys. B **338**, 647 (1990).

[43] S. Chandrasekharan and U.-J. Wiese, Quantum link models: A discrete approach to gauge theories, Nucl. Phys. B **492**, 455 (1997).

[44] R. Brower, S. Chandrasekharan, and U.-J. Wiese, QCD as a quantum link model, Phys. Rev. D **60**, 094502 (1999).

[45] D. Banerjee, M. Dalmonte, M. Müller, E. Rico, P. Stebler, U.-J. Wiese, and P. Zoller, Atomic Quantum Simulation of Dynamical Gauge Fields Coupled to Fermionic Matter: From String Breaking to Evolution after a Quench, Phys. Rev. Lett. **109**, 175302 (2012).

[46] J. C. Halimeh, I. P. McCulloch, B. Yang, and P. Hauke, Tuning the Topological θ-Angle in Cold-Atom Quantum Simulators of Gauge Theories, PRX Quantum **3**, 040316 (2022).

[47] Y. Cheng, S. Liu, W. Zheng, P. Zhang, and H. Zhai, Tunable Confinement-Deconfinement Transition in an Ultracold-Atom Quantum Simulator, PRX Quantum **3**, 040317 (2022).

[48] A. V. Gorshkov, M. Hermele, V. Gurarie, C. Xu, P. S. Julienne, J. Ye, P. Zoller, E. Demler, M. D. Lukin, and A. M. Rey, Two-orbital $SU(N)$ magnetism with ultracold alkaline-earth atoms, Nat. Phys. **6**, 289 (2010).

[49] F. Scazza, C. Hofrichter, M. Höfer, P. C. De Groot, I. Bloch, and S. Fölling, Observation of two-orbital spin-exchange interactions with ultracold SU(N)-symmetric fermions, Nat. Phys. **10**, 779 (2014).

[50] X. Zhang, M. Bishof, S. L. Bromley, C. V. Kraus, M. S. Safronova, P. Zoller, A. M. Rey, and J. Ye, Spectroscopic observation of SU(N)-symmetric interactions in Sr orbital magnetism, Science **345**, 1467 (2014).

[51] M. Takamoto, F.-L. Hong, R. Higashi, and H. Katori, An optical lattice clock, Nature **435**, 321 (2005).

[52] A. D. Ludlow, M. M. Boyd, T. Zelevinsky, S. M. Foreman, S. Blatt, M. Notcutt, T. Ido, and J. Ye, Systematic Study of the ^{87}Sr Clock Transition in an Optical Lattice, Phys. Rev. Lett. **96**, 033003 (2006).

[53] W. Yi, A. J. Daley, G. Pupillo, and P. Zoller, State-dependent, addressable subwavelength lattices with cold atoms, New J. Phys. **10**, 073015 (2008).

[54] J. Sebby-Strabley, M. Anderlini, P. S. Jessen, and J. V. Porto, Lattice of double wells for manipulating pairs of cold atoms, Phys. Rev. A **73**, 033605 (2006).

[55] S. Fölling, S. Trotzky, P. Cheinet, M. Feld, R. Saers, A. Widera, T. Müller, and I. Bloch, Direct observation of second-order atom tunnelling, Nature **448**, 1029 (2007).

[56] L. Tarruell, D. Greif, T. Uehlinger, G. Jotzu, and T. Esslinger, Creating, moving and merging Dirac points with a Fermi gas in a tunable honeycomb lattice, Nature **483**, 302 (2012).

[57] H. Ozawa, S. Taie, T. Ichinose, and Y. Takahashi, Interaction-Driven Shift and Distortion of a Flat Band in an Optical Lieb Lattice, Phys. Rev. Lett. **118**, 175301 (2017).

[58] C. Robens, S. Brakhane, W. Alt, D. Meschede, J. Zopes, and A. Alberti, Fast, High-Precision Optical Polarization Synthesizer for Ultracold-Atom Experiments, Phys. Rev. Appl. **9**, 034016 (2018).

[59] A. Mazurenko, S. Blatt, F. Huber, M. F. Parsons, C. S. Chiu, G. Ji, D. Greif, and M. Greiner, Implementation of a stable, high-power optical lattice for quantum gas microscopy, Rev. Sci. Instrum. **90**, 033101 (2019).

[60] T.-H. Leung, M. N. Schwarz, S.-W. Chang, C. D. Brown, G. Unnikrishnan, and D. Stamper-Kurn, Interaction-Enhanced Group Velocity of Bosons in the Flat Band of an Optical Kagome Lattice, Phys. Rev. Lett. **125**, 133001 (2020).

[61] B. M. Spar, E. Guardado-Sanchez, S. Chi, Z. Z. Yan, and W. S. Bakr, Realization of a Fermi-Hubbard Optical Tweezer Array, Phys. Rev. Lett. **128**, 223202 (2022).

[62] A. W. Young, W. J. Eckner, N. Schine, A. M. Childs, and A. M. Kaufman, Tweezer-programmable 2D quantum walks in a Hubbard-regime lattice, Science **377**, 885 (2022).

[63] M. Höfer, L. Riegger, F. Scazza, C. Hofrichter, D. R. Fernandes, M. M. Parish, J. Levinsen, I. Bloch, and S. Fölling, Observation of an Orbital Interaction-Induced Feshbach Resonance in ^{173}Yb, Phys. Rev. Lett. **115**, 265302 (2015).

[64] A. Goban, R. Hutson, G. Marti, S. Campbell, M. Perlin, P. Julienne, J. D'incao, A. Rey, and J. Ye, Emergence of multibody interactions in a fermionic lattice clock, Nature **563**, 369 (2018).

[65] K. Ono, J. Kobayashi, Y. Amano, K. Sato, and Y. Takahashi, Antiferromagnetic interorbital spin-exchange interaction of ^{171}Yb, Phys. Rev. A **99**, 032707 (2019).

[66] N. D. Lemke, A. D. Ludlow, Z. W. Barber, T. M. Fortier, S. A. Diddams, Y. Jiang, S. R. Jefferts, T. P. Heavner, T. E. Parker, and C. W. Oates, Spin-1/2 Optical Lattice Clock, Phys. Rev. Lett. **103**, 063001 (2009).

[67] C. Weitenberg, M. Endres, J. F. Sherson, M. Cheneau, P. Schauß, T. Fukuhara, I. Bloch, and S. Kuhr, Single-spin addressing in an atomic Mott insulator, Nature **471**, 319 (2011).

[68] C. Gross and W. S. Bakr, Quantum gas microscopy for single atom and spin detection, Nat. Phys. **17**, 1316 (2021).

[69] N. Darkwah Oppong, G. Pasqualetti, O. Bettermann, P. Zechmann, M. Knap, I. Bloch, and S. Fölling, Probing Transport and Slow Relaxation in the Mass-Imbalanced Fermi-Hubbard Model, Phys. Rev. X **12**, 031026 (2022).

[70] M. Endres, H. Bernien, A. Keesling, H. Levine, E. R. Anschuetz, A. Krajenbrink, C. Senko, V. Vuletic, M. Greiner, and M. D. Lukin, Atom-by-atom assembly of defect-free one-dimensional cold atom arrays, Science **354**, 1024 (2016).

[71] Note that here the matter gauge coupling has the same sign on every link, so this model differs from the quantum link model studied in, e.g., Ref. [76]. With this choice, the model has a simpler implementation in the experimental setup that we propose. To obtain couplings with sign $\tilde{s}_{r,r+\hat{x}} = 1$, $\tilde{s}_{r,r+\hat{y}} = (-1)^i$, an approach similar to that of Ref. [89] could be applied.

[72] C. Laflamme, W. Evans, M. Dalmonte, U. Gerber, H. Mejía-Díaz, W. Bietenholz, U.-J. Wiese, and P. Zoller, $\mathbb{C}\mathrm{P}(N-1)$ quantum field theories with alkaline-earth atoms in optical lattices, Ann. Phys. (NY) **370**, 117 (2016).

[73] R. Verresen, M. D. Lukin, and A. Vishwanath, Prediction of Toric Code Topological Order from Rydberg Blockade, Phys. Rev. X **11**, 031005 (2021).

[74] P. S. Tarabunga, F. M. Surace, R. Andreoni, A. Angelone, and M. Dalmonte, Gauge-Theoretic Origin of Rydberg Quantum Spin Liquids, Phys. Rev. Lett. **129**, 195301 (2022).

[75] R. Verresen and A. Vishwanath, Unifying Kitaev Magnets, Kagomé Dimer Models, and Ruby Rydberg Spin Liquids, Phys. Rev. X **12**, 041029 (2022).

[76] D. Banerjee, M. Bögli, M. Dalmonte, E. Rico, P. Stebler, U.-J. Wiese, and P. Zoller, Atomic Quantum Simulation of U(N) and SU(N) Non-Abelian Lattice Gauge Theories, Phys. Rev. Lett. **110**, 125303 (2013).

[77] E. Zohar, J. I. Cirac, and B. Reznik, Cold-Atom Quantum Simulator for SU(2) Yang-Mills Lattice Gauge Theory, Phys. Rev. Lett. **110**, 125304 (2013).

[78] L. Tagliacozzo, A. Celi, P. Orland, M. Mitchell, and M. Lewenstein, Simulation of non-Abelian gauge theories with optical lattices, Nat. Commun. **4**, 1 (2013).

[79] K. Stannigel, P. Hauke, D. Marcos, M. Hafezi, S. Diehl, M. Dalmonte, and P. Zoller, Constrained Dynamics via the Zeno Effect in Quantum Simulation: Implementing Non-Abelian Lattice Gauge Theories with Cold Atoms, Phys. Rev. Lett. **112**, 120406 (2014).

[80] A. Mezzacapo, E. Rico, C. Sabín, I. L. Egusquiza, L. Lamata, and E. Solano, Non-Abelian SU(2) Lattice Gauge Theories in Superconducting Circuits, Phys. Rev. Lett. **115**, 240502 (2015).

[81] E. Rico, M. Dalmonte, P. Zoller, D. Banerjee, M. Bögli, P. Stebler, and U.-J. Wiese, SO(3) "nuclear physics" with ultracold gases, Ann. Phys. (NY) **393**, 466 (2018).

[82] V. Kasper, T. V. Zache, F. Jendrzejewski, M. Lewenstein, and E. Zohar, Non-Abelian gauge invariance from dynamical decoupling (2020), ArXiv:2012.08620.

[83] Z. Davoudi, I. Raychowdhury, and A. Shaw, Search for efficient formulations for Hamiltonian simulation of non-Abelian lattice gauge theories, Phys. Rev. D **104**, 074505 (2021).

[84] D. González-Cuadra, T. V. Zache, J. Carrasco, B. Kraus, and P. Zoller, Hardware efficient quantum simulation of non-Abelian gauge theories with qudits on Rydberg platforms (2022), ArXiv:2203.15541.

[85] S. Kivelson, Wannier functions in one-dimensional disordered systems: Application to fractionally charged solitons, Phys. Rev. B **26**, 4269 (1982).

[86] T. Uehlinger, G. Jotzu, M. Messer, D. Greif, W. Hofstetter, U. Bissbort, and T. Esslinger, Artificial Graphene with Tunable Interactions, Phys. Rev. Lett. **111**, 185307 (2013).

[87] N. Marzari and D. Vanderbilt, Maximally localized generalized Wannier functions for composite energy bands, Phys. Rev. B **56**, 12847 (1997).

[88] N. Marzari, A. A. Mostofi, J. R. Yates, I. Souza, and D. Vanderbilt, Maximally localized Wannier functions: Theory and applications, Rev. Mod. Phys. **84**, 1419 (2012).

[89] D. Jaksch and P. Zoller, Creation of effective magnetic fields in optical lattices: The Hofstadter butterfly for cold neutral atoms, New J. Phys. **5**, 56 (2003).